CHANDRA SPECTROSCOPY OF MAXI J1305−704: DETECTION OF AN INFALLING BLACK HOLE DISK WIND?

J. M. MILLER[1], J. RAYMOND[2], T. R. KALLMAN[3] D. MAITRA[1], A. C. FABIAN[4], D. PROGA[5] C. S. REYNOLDS[6], M. T. REYNOLDS[1], N. DEGENAAR[1,7], A. L. KING[1], E. M. CACKETT[8], J. A. KENNEA[9], A. BEARDMORE[10]

Submitted to ApJ

ABSTRACT

We report on a *Chandra*/HETG X-ray spectrum of the black hole candidate MAXI J1305−704. A rich absorption complex is detected in the Fe L band, including density–sensitive lines from Fe XX, XXI, and XXII. Spectral analysis over three bands with photoionization models generally requires a gas density of $n \geq 10^{17}$ cm^{-3}. Assuming a luminosity of $L = 10^{37}$ erg s^{-1}, fits to the 10–14 Å band constrain the absorbing gas to lie within $r = 3.9 \pm 0.7 \times 10^3$ km from the central engine, or about $r = 520 \pm 90$ ($M/5\ M_\odot$) r_g, where $r_g = GM/c^2$. At this distance from the compact object, gas in Keplerian orbits should have a gravitational red-shift of $z = v/c \simeq 3 \pm 1 \times 10^{-3}$ ($M/5\ M_\odot$), and any tenuous inflowing gas should have a free–fall velocity of $v/c \simeq 6 \pm 1 \times 10^{-2}$ ($M/5\ M_\odot$)$^{1/2}$. The best-fit single-zone photoionization models measure a red-shift of $v/c = 2.6 - 3.2 \times 10^{-3}$. Models with two zones provide significantly improved fits; the additional zone is measured to have a red-shift of $v/c = 4.6–4.9 \times 10^{-2}$ (models including two zones suggest slightly different radii and may point to lower densities). Thus, the shifts are broadly consistent with the photoionization radius. The results may be explained in terms of a "failed wind" like those predicted in some numerical simulations. We discuss our results in the context of accretion flows across the mass scale, and the potential role of failed winds in black hole state transitions.

Subject headings: Black hole physics – relativity – stars: binaries – physical data and processes: accretion disks

1. INTRODUCTION

Ionized X-ray absorption lines are now observed in high resolution X-ray spectra from a fairly large number of X-ray binaries. In some cases, the lines are observed close to their rest wavelengths, and likely arise in the coronal interstellar medium (e.g. Juett et al. 2006) or in ionized gas within the binary (Diaz-Trigo et al. 2006). When such lines are significantly blue-shifted, however, they likely trace outflowing disk winds. Ionized X-ray winds have now been observed in both stellar-mass black hole systems (e.g. Miller et al. 2006a,b; Kubota et al. 2007; Miller et al. 2008; Ueda, Yamaoka, & Remillard 2009; Neilsen & Lee 2009; King et al. 2012) and in neutron star binaries (Ueda et al. 2004, Miller et al. 2011). These winds may eject more matter than is able to accrete onto the compact object, making their study essential to a complete picture of disk accretion.

Understanding the physical mechanisms by which the winds are launched, driven, and modulated may be key to revealing the physics of disk accretion itself (Miller et al. 2006a,

2008), as well as black hole state transitions (e.g. Miller et al. 2008, Neilsen & Lee 2009, Ponti et al. 2012, Miller et al. 2012). Global studies of disk winds and their relationship to jet outflows offer one important angle on this problem (e.g. King et al. 2013). Another angle is available when X-ray spectra contain density-sensitive lines that can help to accurately reveal the launching radius and mass outflow rate of the wind. In such cases, it is possible to distinguish thermal driving (e.g. Begelman, McKee, & Shields 1983) from magnetic driving mechanisms (e.g. Blandford & Payne 1982, Proga 2003; also see Reynolds 2012).

Although He-like triplets and emission line ratios can give gas densities, emission can originate in regions unrelated to a wind. This is particularly problematic in the case of AGN, where illumination of the torus can give rise to He-like triplets that do not necessarily reflect the state of gas closer to the black hole. Spectra observed from X-ray binaries, in contrast, typically span a far narrower range in ionzation, and it is particularly unlikely that multiple regions may contribute to a line spectrum in systems with low mass (e.g. solar mass) companions. Robust wind constraints can be obtained using the density-sensitive Fe XXII line pair (11.77Å, 11.92Å; see Mauche, Liedahl, & Fournier 2003); blue-shifted detections in the spectrum of GRO J1655−40 permitted strong wind constraints in that system, and a weak detection of the line pair was claimed in NGC 4051 (Miller et al. 2008; King, Miller, Raymond 2012). At higher densities, it is possible to use the ratio of Fe XXI lines (12.259 Å and 12.325 Å) as a density diagnostics (see, e.g., King, Miller, & Raymond 2012). Especially in X-ray binaries, the use of such lines is partly dependent on observing sources with a modest column density through the ISM, in order to preserve flux in the Fe L band.

MAXI J1305−704 was discovered on 09 April 2012, at a flux of 30 mCrab in the 4–10 keV band (Sato et al. 2012). The low column density along this line of sight enables opti-

[1] Department of Astronomy, The University of Michigan, 500 Church Street, Ann Arbor, MI 48109, jonmm@umich.edu
[2] Harvard-Smithonian Center for Astrophysics, 60 Garden Street, Cambridge, MA, 02138
[3] NASA Goddard Space Flight Center, Code 662, Greedbelt, MD, 20771, USA
[4] Institute of Astronomy, University of Cambridge, Madingley Road, Cambridge CB3 OHA, UK
[5] Department of Physics, University of Nevada, Las Vegas, Las Vegas NV, 89154
[6] Department of Astronomy, University of Maryland, College Park, MD, 20742-2421
[7] Hubble Fellow
[8] Department of Physics and Astronomy, Wayne State University, Detroit, MI, 48201
[9] Department of Astronomy & Astrophysics, The Pennsylvania State University, 525 Davey Lab, University Park, PA, 16802
[10] Department of Physics and Astronomy, University of Leicester, Leicester, LE1 7RH, UK

cal observations in many bands, and a counterpart was soon identified (Greiner, Rau, & Schady 2012). It is particularly notable that the source colors, optical spectrum, and hard X-ray rise are very similar to the properties observed from the well-known black hole XTE J1118+480 (Greiner, Rau, Schady 2012; Charles et al. 2012). MAXI J1305−704 was also quickly detected in radio bands (Coriat et al. 2012). This is also weakly suggestive of a black hole system, as black holes appear to be more luminous in radio than neutrons stars (Migliari & Fender 2006). Suwa et al. (2012) noted that outburst evolution and states observed from MAXI J1305−704 are also suggestive of a black hole, but cannot rigidly exclude a neutron star. The source has been observed to display X-ray flux dips (see, e.g. Kuulkers, Motta, & Belloni 2012), indicating a relatively high inclination, and permitting a binary period measurement of 9.74 ± 0.04 hours (Shidatsu et al. 2013). Thus, although there are indications of a black hole, the distance to MAXI J1305−704, and the nature of the compact object are currently unknown.

A snapshot exposure with *Swift* detected an Fe K absorption line in the persistent emission of MAXI J1305−704, as well as some preliminary indications for absorption in the Fe L band (Miller et al. 2012b). We then requested a *Chandra* observation with the particular aim of detecting a disk wind and Fe XXII absorption lines. A preliminary report on the *Chandra* spectrum is given in ATEL 4191 (Miller et al. 2012c).

2. OBSERVATIONS AND DATA REDUCTION

MAXI J1305−704 was observed with *Chandra* for 30.0 ks starting on 2012 August 02 at 12:22:17 (UT). The incident flux was dispersed onto the ACIS-S array using the HETG. The ACIS array was operated in the "faint" data mode as the source was not as bright as many X-ray binaries, which often require the array to be operated in "continuous clocking" mode. The observation was executed using the MAXI coordinates (13h 05m 39.9s, −70° 24' 54"; Sato et al. 2012). However, an improved source position was later obtained in a *Swift* imaging observation (13h 06m 55.53s, −70° 27' 01.8"; Kennea et al. 2012). Thus, the true source position is approximately 6.7' from the position at which *Chandra* pointed. The roll angle of the observatory was fortuitous, however, and the source was not only imaged on the ACIS-S array, but on the S3 chip.

All of the *Chandra*-specific data reduction tasks in this paper were performed using CIAO version 4.4.1 and the latest associated calibration database files. Other tasks were accomplished using the tools and calibration files available in the HEASOFT suite, version 6.12. Spectral fits were made using XSPEC version 12.7.1 (Arnaud & Dorman 2000). The spectrum is extremely sensitive so we employed χ^2 fitting statistics and calculated significance levels using the F-test. All errors quoted in this work correspond to 1σ confidence limits.

The zeroth order image of MAXI J1305−704 is extended into an elliptical shape owing to its off-axis position. We therefore investigated whether or not the automatic processing used to create level-2 event files had correctly identified the centroid of the zeroth order image. Owing to the fact that this position is used to set the wavelength grid for the MEG and HEG spectra, the wavelengths of strong lines in opposing spectral orders (e.g. +1 and −1) can be used to check the zeroth order position. Discrepancies in the wavelengths of strong lines were found, and so we iteratively adjusted the position of the zeroth order, produced new event files, spectral files (using "acis_process_events", "tgdetect",

"tg_create_mask", "tg_resolve_events", and "tgextract"), and responses (using "mkgrmf" and "fullgarf"), until agreement was found between opposing first-order spectra in both the MEG and HEG. The "add_grating_orders" tools was used to combine the first-order MEG and HEG spectra and responses prior to analysis. One arm of the HEG is truncated owing to the offset pointing, and the remaining arm lacks the sensitivity for line studies in the Fe K band. The collecting area of the MEG is higher than the HEG in the Fe L band even in a nominal observation. For these reasons, the analysis below is restricted to the combined first-order MEG spectrum of MAXI J1305−704.

Zeroth order spectra and response files were extracted using the "specextract" script. The entirety of the zeroth order image was extracted using a large elliptical region. As expected based on the source image, fits to this extraction reveal the effects of photon pile-up, most promininently in the high energy band where artificially–summed events are registered as single photons. While the continuum is affected, the centroid energy of absorption lines is robust against pile-up, and this later serves as a check on the results obtained from the dispersed spectrum.

3. ANALYSIS AND RESULTS

3.1. *Light Curve*

As noted above, MAXI J1305−704 is known to be a "dipping" source, based on numerous *Swift* observations. Flux dips are most often observed in systems in which the line of sight is close to the plane of the accretion disk, likely signaling that the dips are caused by material just above the outer disk (e.g. Diaz-Trigo et al. 2006). This line of sight is fortuitous for efforts to study equatorial winds (Miller et al. 2006b, 2008; Ponti et al. 2012). We therefore extracted and examined the lightcurve of the dispersed spectra. Using "dmextract", we extracted the first-order MEG and HEG events in the 0.3–10.0 keV range, and summed the light curve into 10 s bins for visual clarity (see Figure 1). The flux is found to decrease by a factor of $\simeq 2$ in the final few kiloseconds of the observation, with marginal evidence of a short, weak dip event about 28 ks into the observation, lasting less than 1 ks. If the slow decline at the end of the observation is the start of a dip event, it is much weaker than the strong, sharp dips reported by e.g. Kennea et al. (2012), and unlikely to have a strong impact on the spectrum. We therefore proceeded to analyze the time-averaged spectrum gathered from the entire *Chandra* observation.

3.2. *The First-Order MEG Spectrum*

We considered the combined first-order MEG spectrum of MAXI J1305−704 in the 8–19.5 Å band, and in selected slices of this range. This full band is clearly dominated by strong – and sometimes blended – Fe L absorption lines. At longer wavelengths, the spectrum is attenuated by interstellar absorption. At shorter wavelengths, there are sharp changes in the instrument response owing to the off-axis nature of the source position, and resulting consequences for chip gaps and other features. Though this is a limited band and there is evidence of absorption in e.g. the 6–8 Å band as well, the 8–19.5 Å band effectively captures the Fe L absorption seen with *Swift*.

The spectral continuum is not the focus of our investigation; we regard the continuum as largely fiducial as the large offset pointing may cause flux calibration uncertainties. How-

ever, a few notes are required. All spectral fits to the MEG spectrum were made using the "tbabs" absorption model with corresponding atomic cross-sections and abundances (Wilms, Allen, & McCray 2000). The effective neutral hydrogen column density along the line of sight to MAXI J1305−704 is very low and difficult to constrain; however, a value of $N_H = 1.5 \times 10^{21}$ cm^{-2} permits a reasonable characterization of the low-energy spectrum. This value was fixed in all fits. The MEG spectrum is dominated by soft, thermal emission that can be fit with a $kT \simeq 1$ keV disk blackbody model (Mitsuda et al. 1984). A hard spectral component is required and was characterized with a simple power-law model; the spectral index of this model depends on the band under consideration. Over the 8–19.5 Å range, a soft index of $\Gamma \simeq 3$ yields good fits. This continuum is broadly similar to that observed in GRO J1655−40 when a dense, ionized, magnetically-driven wind was detected (Miller et al. 2006b, 2008; Kallman et al. 2009; also see Neilsen & Homan 2009 and Neilsen 2013), and also similar to the soft, disk–dominated continua found as winds were launched in H 1743−322 (Miller et al. 2006), GRS 1915+105 (Ueda et al. 2009), and IGR J17091−3624 (King et al. 2012). Last, we found that two broad ($\sigma \simeq 0.1$ keV) Gaussian emission functions with centroids between 0.7–0.8 keV and 1.2–1.3 keV generally improved the fits. These lines wer also detected in a *Suzaku* spectrum of MAXI J1305−704 (Shidatsu et al. 2013). They are broadly similar to lines reported in compact X-ray binaries by Madej et al. (2010) and Madej & Jonker (2011), and interpreted as relativistic disk lines. We suggest that relativistic O VIII and Fe L lines may provide a reasonable interpretation of the lines we have detected (also see Shidatsu et al. 2013). They are adequately fit with Gaussians and we defer more detailed analysis in order to focus on the rich absorption spectrum.

Fits to the 8–19.5 Å band with a $kT = 1.0$ keV disk plus blackbody and power-law model do not give formally acceptable fits, but do allow for a basic flux characterization. Using this model, a flux of $F = 3.1 \times 10^{-9}$ erg cm^{-2} s^{-1} is implied for the 0.3–10.0 keV band. The source is not positioned close to the Galactic Center, but the distance to Galactic Center is a useful benchmark. This flux gives a luminosity of $L = 2.7 \times 10^{37}(d/8.5 \text{ kpc})^2$ erg s^{-1}. Thus, even for fairly large distances, the luminosity of MAXI J1305−704 is unlikely to greatly exceed $L = 10^{37}$ erg s^{-1}, and this value gives a useful standard for eventual scaling when the distance is known.

Unlike H 1743−322 and IGR J17091−3624, where only two lines are detected in the Fe K band, and unlike GRO J1655−40 and GRS 1915+105, where a high ionization parameter spurred absorption across the full soft X-ray band, the absorption in MAXI J1305−704 is strongly concentrated in the Fe L band, near to 1 keV (1 keV × 1 Å = 12.39852), though Fe K absorption is also evident. Thus, whereas phenomenological modeling of the absorption lines with simple Gaussian functions was sensible in other sources, the presence of multiplets and line blends limits the utility of simple Gaussian functions in describing the spectrum of MAXI J1305−704. Moreover, in this situation, the transition that one might assign to a given line can depend on the gas density and ionization, which requires careful modeling of numerous lines using a self-consistent model.

The density-sensitive Fe XXII lines at 11.77 Å and 11.92 Å are important exceptions. The ratio of these lines is a density diagnostic for $n \geq 10^{12}$ cm^{-3} (e.g. Mauche, Liedahl,

& Fournier 2003). Even visual inspection of the lines confirms that the 11.92 Å line is stronger than the 11.77 Å line in the spectrum of MAXI J1305−704, in contrast to the ratio found in GRO J1655−40 and NGC 4051 (King, Miller, & Raymond 2012). We constructed a crude power-law model of the continuum in the 11.2–12.7 Å band and characterized the absorption with Gaussian functions in order to make fits to the Fe XXII lines. Via the Gaussian fits, the 11.92 /11.77 flux ratio exceeds 1.6; CHIANTI simulations presented in Figure 4 of Miller et al. (2008) show that this requires a density of $n > 10^{15}$cm^{-2}.

3.3. *Photoionization Modeling*

Owing to the complexity of the observed spectrum, we calculated a large grid of photoionization models using XSTAR version 221bn15 (Kallman & Bautista 2001). Based on our broad-band spectral fits, we calculated models assuming a simple, unabsorbed, $kT = 1.0$ keV spectrum incident upon the gas, with a luminosity of $L = 1.0 \times 10^{37}$ erg s^{-1}. The detection of flux dips in *Swift* monitoring of MAXI J1305−704 demands a high inclination; an equatorial wind or flow is also indicated by the lack of strong, narrow emission lines. Their absence indicates the lack of dense material above our line of sight that could reprocess the X-rays and contribute emission lines. For simplicity and consistency with other sources (see, e.g., King et al. 2013), our XSTAR models assumed a covering factor of $\Omega/4\pi = 0.5$. Solar abundances were assumed for all elements and all models. Numerous tests indicated that a turbulent velocity of $v = 700$ km/s gives the best description of the data, and this was then assumed in all models.

As noted above, when the density-sensitive Fe XXII lines are modeled with Gaussian functions, their ratio of $\simeq 1.6$ implies a density of at least $n \geq 10^{15}$ cm^{-3} (Miller et al. 2008). Nevertheless, in order to test the sensitivity of the spectrum to different densities, we constructed models with $n = 10^{13}, 10^{14}, 10^{15}, 10^{16}, 10^{17},$ and 10^{18} cm^{-3}. The models with $n \leq 10^{15}$ cm^{-3} produced poor fits to the spectrum of MAXI J1305−704. In particular, those models over-predicted many Fe L lines, and predicted Fe XXII lines where the 11.77Å line was much stronger than the 11.92Å line. We therefore constructed a grid of 8000 models using a computing cluster, spanning $2.0 \leq \log(\xi) \leq 4.0$, 5×10^{21} cm$^{-2} \leq N_H \leq 5 \times 10^{23}$ cm^{-2}, and 10^{16} cm$^{-3} \leq n \leq 10^{18}$ cm^{-3}.

We explored fits over three different wavelength regions, selected to focus narrowly on the Fe XXI and Fe XXII lines (11.2–13.2Å), to include the Fe XXII lines and nearby Fe L shell lines (10.0–14.0Å), and the full MEG first-order band considered in this work (8.0–19.5Å). In the narrow bands, the continuum was fit with phenomenological power-law models; in the last (widest) band, more physical disk blackbody and power-law models were combined to describe the continuum. In each case, the corresponding emission line spectrum generated by XSTAR was added to the continuum, with $n, N, \xi,$ and v all fixed to the values deterned by the absorption component. The addition of the corresponding emission line spectra does not substantially alter the fits; it is simply a measure taken to ensure internal consistency. The results of these fits are given in Table 1. The lines that contribute most to the absorption spectrum are given in Table 2. Fits to specific wavelength ranges, and comparisons between specific models, are shown in Figures 2, 3, and 4.

In all fits with a single-zone photoionized absorber, the

spectrum requires a very high density. In fits to the 10–14 Å region, for instance, Model 5 ($n = 6 \pm 1 \times 10^{17}$ cm^{-3}) is a 5.7σ improvement over Model 7 (density fixed at $n = 1.0 \times 10^{16}$ cm^{-3}). Some lines – especially the cluster near to 13Å – appear to require an extremely specific set of parameters, and are therefore better modeled in fits to a narrow wavelength range. The O VIII Ly-α and Ly-β lines are generally fit poorly by the models that fit the Fe L shell lines well. It is possible that a lower density and higher ionzation absorber can fit these lines better. However, fits with a single zone where log(n)= 13.0, although they do push to log(ξ) $\geq$ 4, are worse than Model 5 (see Table 1) by a margin of several hundred in χ^2. Therefore, it appears possible that abundance variations may account for the poor fits, rather than incorrect descriptions of the density and ionization. It is also possible that a model with a large number of absorption zones, or a continuous range of zones, might be able to fit both the Fe L lines and O VIII lines without abundance variations.

The photoionization models are driven toward very high density values partly by the need to fit other density–sensitive lines. Just as Fe XXII absorption can reveal the presence of the excited fine structure level $2p\ ^2P_{3/2}$, providing density measurements in the 10^{14} to 10^{15} range, the population of the $2p^2\ ^1D$ and ^1S levels of Fe XXI and the $2p^3\ ^2D$ and ^2P levels of Fe XX provide diagnostics for densities above $n \geq 10^{17}$ cm^{-3}. The Fe XXI lines (12.259 Å and 12.325 Å; see Table 2) are more prominent in the spectrum of MAXI J1305−704. Their utility of Fe XXI lines was initially demonstrated in King, Miller, & Raymond (2012), though in that work the sensitivity to densities below $n = 10^{14}$ cm^{-3} comes from the $2p2\ ^3P_2$ level, which has a lower critical density than the $2p2\ ^1D_1$ level that is important for MAXI J1305−704. Whereas fits with Gaussians are unable to determine the relative contributions of Fe XXI and Ne X Ly-series lines in his range, the XSTAR photoionization models can do this self–consistently. Contributions from the Fe XX and Fe XXI lines listed in Table 2 are partly responsible for the statistically significant improvements found in in Table 1, when comparing single–zone models with $n \geq 10^{17}$ cm^{-3} to those with a fixed value of $n = 10^{16}$ cm^{-3}.

In order to be sure that the fitting process did not miss subtle minima that would have permitted a low value for the gas density, we explored a broad range of fits. Grids of 25 pairings of column density ($N_H = 5.0 \times 10^{21}, 1 \times 10^{22}, 5 \times 10^{22}, 1 \times 10^{23}, 5 \times 10^{23}$ cm^{-2}) and the ionization parameter (logξ = 2.5, 3.0, 3.5, 4.0, 4.5) were fit to the 10–14 Å range, for four different values of the gas density ($n = 10^{13}, 10^{14}, 10^{15}, 10^{16}$ cm^{-3}). The results of this check are displayed in Figure 5. The size of the plotting symbol in Figure 5 encodes the change in the fit statistic, $\Delta(\chi^2)$, for each of the 100 different points considered. Clearly, plausible models with lower density simply do not give fits as good as models with high values of the gas density.

The distance between the central engine and the absorbing gas is contained in the definition of the ionization parameter, $\xi = L/nr^2$. If we take the model for the 10–14Å range as repreresenative, $r = 3.9 \pm 0.7 \times 10^8$ cm or $r = 3.9 \pm 0.7 \times 10^3$ km. Nominally, this radius does not rigidly exclude a geometry like the boundary layer on an accreting white dwarf; however, this explanation of the absorption region is unlikely given the similarity of optical spectra of MAXI J1305−704 to optical

spectra of confirmed black holes such as XTE J1118+480 (e.g. Charles et al. 2012). This distance corresponds to $r = 1300 \pm 200\ GM/c^2$ assuming that the compact object is an $M = 2.0\ M_\odot$ neutron star, or $r = 520 \pm 90\ GM/c^2$, assuming an $M = 5M_\odot$ black hole primary.

In each wavelength range, we also considered fits with two absorbing zones (see Table 1, and Figures 3 and 4). These models yielded enormous statistical improvments. In fits to the 10–14 Å range, for instance, the best–fit two–zone model (Model 8 in Table 1) is an enormous ($>> 8\sigma$) improvement over the best-fit single–zone model (Model 5). A direct comparision of these models is shown in Figure 3. The specific effect of the velocity shifts is shown in Figure 4. Most notably, in each wavelength range, the second absorption zone is more strongly red-shifted, with values approaching $v/c = 0.05$ (see Table 1).

The XSTAR code we have used does not include the recent results on the suppression of dielectronic recombination at high densities by Nikolic et al. (2013). The recombination rates of the Fe L-shell ions are reduced by factors of $\leq$ 2 at densities above 10^{17} cm^{-3}, and since the ionization parameter determined from the spectral fits is determined largely by the relative fractions of these ions, the ionization parameter ξ is even smaller than the values given by the fits. That would imply that the values of r quoted in Table 1 should be increased by a factor of $\sqrt{(2)}$; however, this is easily within the uncertainty in the X-ray luminosity.

Several effects can potentially contribute to the breadth of the absorption lines in the spectrum of MAXI J1305−704, including a degree of instrumental broadening (see below). Given the small absorption radius inferred from even single–zone fits, it is interesting to consider whether or not tangential velocities have been encoded into absorption. Doppler–split line pairs are not typically seen in X-ray absorption as the central engine is taken to be a point source compared to the absorbing region. Simple arguments show that shifts of $v/c \simeq h\sin(\theta)/w^{3/2}$ are expected (where h is the size of the hard x-ray central engine, w is the size of the wind launching region, and θ is the inclination angle measured relative to the disk normal). Standard disk models predict that emissivity drops sharply with radius (Shakura & Sunyaev 1973), and new work suggests that coronae are also centrally–concentrated (e.g. Reis & Miller 2013). Taking $h = 10GM/c^2$ and $\theta \simeq 60°$, shifts of $v = \pm 400$ km/s are expected. This is broadly consistent with the width of the lines detected in MAXI J1305−704, and also consistent with the turbulent velocity assumed in our XSTAR models ($v = 700$ km/s). The nominal value of $N/n = \Delta(r)$ for the single zone models in Table 1 can be as small as 1 km. It is possible that in the limit of zero intrumental broadening due to the pointing offset (see below), or at higher spectral resolution (such as that available with *Astro-H*, Takahashi et al. 2012), Doppler-split line pairs would be detected.

However, numerous instrumental and astrophysical effects may serve to prevent Doppler-split lines, and/or their detection, even in this spectrum. Artificial line broadening due to the telescope pointing offset may have served to blur away the velocity structure. Optical depth effects can spoil line splitting signatures. Very small values of $\Delta(r)$ partly rely on the assumption of a unity filling factor; if the gas is sparse and clumpy – as might be the case if it is affected by radiation pressure – values of $\Delta(r)$ could be much larger. Moreover, this analysis has only focused on a very small wavelength region, dominated by transitions to and from the Fe L shell, and

thus centered on a narrow range in ionization. An excellent HEG specrum in the Fe K band could have detected absorption from very highy ionized gas that would have implied a much larger wind depth. The two-zone models detailed in Table 1 may already supply a partial solution: Models 4, 8, and 12 give radii that differ by an appreciable factor, and strongly suggest that $\Delta(r)/r$ is not very small. In this regime, Doppler-split lines from larger radii would fill-in pairs from smaller radii, and spoil the signature of rotation.

While the continuum shape and flux of the zeroth-order spectrum are affected by pile-up, the centroid energy of discrete atomic features within the ACIS S3 CCD spectrum should be relatively unaffected, and absorption in the Fe K band can serve as a check on the need for a more red-shifted component in the absorption spectrum. We therefore fit the zeroth order ACIS-S3 spectrum of MAXI J1305−704. A clear broad absorption trough – likely composed of Fe XXV and Fe XXVI lines – is clearly present, consistent with the prior *Swift* spectrum of MAXI J1305−704. In order to focus the action of the XSTAR photoionization models on the Fe K region, we restricted our fits to the 3.0–10.0 keV band. The spectrum suffers from pile-up, and while a disk blackbody model gives temperatures near to 1 keV, an additional power-law component with a negative spectral index. Thus, at least the high energy part of the spectral model must be considered fiducial.

The broad absorption feature in the zeroth-order spectrum can be fit with a single Gaussian function, with a centroid energy of E= 6.73 ± 0.02 keV and a FWHM of 0.38 ± 0.04 keV. This nominally indicates a blue-shift, but this may be artificial. It is very difficult to produce only Fe XXV or Fe XXVI in isolation (see, e.g. Kallman & Bautista 2001), and this line is too broad to be composed of a single line, if the feature bears any relation to the lines in the MEG spectrum. Fits to these two lines with a single Gaussian function – even if the two are slightly red-shifted, can result in a net blue-shift. The relative strength of Fe XXV and Fe XXVI lines cannot be determined using Gaussian models for the zeroth-order spectrum, and many different line flux ratios could be assumed. It is notable that a simple assumption – two Gaussians required to maintain the energy offset measured between Fe XXV and XXVI in the laboratory, with line widths required to be equivalent – yields red-shifted lines at E= 6.62 ± 0.02 keV and E= 6.89 ± 0.02 keV. This is not proof of a red-shift in the zeroth-order data, but it serves to illustrate a potential consistency even via phenomenological fits."

The results of several fitting experiments are given in Table 1 and shown in Figure 6. As an initial baseline, we fit the spectrum with a single-zone absorber, with parameters tied to those of the less shifted component revealed in the MEG spectrum over the 8–19.5 Å band. Adding a second absorber then gives an improvement significant at the 6σ level of confidence based on an F-test (Model 15 versus Model 13 in Table 1), and requires a red shift of $v/c = 0.022(1)$. We then made fits to the spectrum with a single-zone absorber, with only the density fixed (since this cannot be constrained directly in the Fe K band). Adding a second absorption zone is then significant at the 4.2σ level of confidence (Model 16 versus Model 14 in Table 1), and a red-shift of $v/c = 0.021(3)$ is measured for the second zone. These are necessarily limited fitting experiments, and CCD-resolution spectra are not as suited to this purpose as dispersed spectra. However, these results do suggest that a second, more highly red-shifted absorption zone may also be indicated in the Fe K band.

3.4. *Ray tracing*

The off-axis telescope does serve to broaden the zeroth-order image, resulting in reduced resolution in the dispersed X-ray spectrum. In addition, it is possible that the offset has induced artificial red-shifts through distortions to the wavelength grid. To understand the effects of the large offset pointing on the observed spectrum, we ran simulations using version 4.0 of MARX. This package contains detailed, CIAO–independent characterizations of the *Chandra* mirrors, detectors, and gratings instruments. Photons from any input spectral form can be traced through their interactions with the telescope and detectors, and compiled into a simulated data file. Regular CIAO tools can then be run on the simulated data, and simulated data products and spectra can be compared to the observed spectra.

The actual pointing position of the *Chandra* observation was used in the MARX simulation. The true source position was placed off-axis in the simulation, again exactly as per the actual observation. Even the spacecraft roll angle was selected to match the actual observation. A simple power-law input spectrum with three strong Gaussian absorption lines (0.900 keV, 1.000 keV, 1.100 keV, each with $\sigma = 5.0 \times 10^{-3}$ keV) was simulated in XSPEC at very high resolution, and then normalized to have the same photon flux as the actual *Chandra* observation. Assuming a point source for MAXI J1305−704, MARX passed rays from this distribution through models of the HRMA, HETG, and ACIS-S array. The resultant event list was reduced in exactly the manner that actual data would be reduced, using the same CIAO tools.

Fitting the MEG−1 and MEG+1 orders extracted from simulated data separately, we find no evidence of a mismatch in the wavelength grid. Nor was evidence of a net red-shift found. Indeed, the centroid of each line in the simulated spectra was found to match the input value to within 0.001 keV. (Here it is worth noting that an incorrect zeroth order position in deriving the real and simulated spectra would result in line broadening or splitting, not in a net shift.) However, there is evidence of line broadening due to the offset pointing, and the effect may be more pronounced at shorter wavelengths. Fits to the simulated MEG−1 spectrum, for instance, gave values of $\sigma = 6.2(2) \times 10^{-3}$ keV, $\sigma = 7.4(2) \times 10^{-3}$ keV, and $\sigma = 8.1(2) \times 10^{-3}$ keV, for the lines inserted at 0.900 keV, 1.000 keV, and 1.100 keV, respectively (recall that $\sigma_{\mathrm{input}} = 5.0 \times 10^{-3}$ keV).

In summary, simulations with MARX suggest that the observed lines are likely to be artificially broadened to some degree, perhaps by 20–50%, but that the observed red-shifts are likely astrophysical. This possibility of wavelength–dependent artificial line broadening is in some conflict with the observed spectrum of MAXI J1305−704: lines at shorter wavelengths do not appear to be systematically broader than lines at shorter wavelengths. It is possible that astrophysical complications, such as a range of ionization parameters, distances, and turbulent velocities, may have served to obscure any wavelenth–dependent instrumental broadening. Although the simulated spectrum does not show a net red-shift, our view is that an instrumental origin remains as a remote possibility. MARX is extremely powerful, but it is only as good as the intrument characterizations, and it is possible that our observation pushes beyond the data on which MARX is based.

4. DISCUSSION

We have analyzed a *Chandra* high-resolution X-ray spectrum of the transient X-ray binary MAXI J1305−704 in outburst. A snapshot CCD spectrum of the source obtained with the *Swift*/XRT detected Fe K absorption, and also suggested strong Fe L shell absorption. The *Chandra* spectrum dramatically confirms this suggestion, revealing an especially complex and rich array of absorption lines from Fe XIX–XXIV, as well as H-like and He-like charge states of O and Ne, and likely also Na and Mg (see Tables 1 and 2, and Figures 2, 3, and 4). The MEG spectrum is extremely sensitive and complex; the rich wind absorption spectrum detected in GRO J1655−40 may be the most natural point of comparison. In both cases, the situation is more similar to fitting UV spectra from quasars rather than typical X-ray binary spectra: formally acceptable fits with self-consistent photoionization models are made impossible by the quality of the data (see, e.g., Miller et al. 2006, 2008; Kallman et al. 2009; Neilsen & Homan 2012). None of the models presented in Table 1 are formally acceptable. However, the relative quality of different models can still be evaluated via changes in the χ^2 fitting statistic.

Most importantly, the density–sensitive Fe XXII line pair at 11.77 Å and 11.92 Å is detected (see Figures 3 and 4), and the flux ratio of these lines requires a very high density. Even a crude comparison to prior calculations suggests $n > 10^{15}$ cm^{-2} (see, e.g., Miller et al. 2008). For an assumed luminosity of $L = 10^{37}$ erg s^{-1} and an ionization parameter of $\xi \simeq 2$, this density limit requires $r \leq 10^{10}$ cm^{-2}. Detailed fits with a very large and finely-spaced set of XSTAR photoionization models finds $n \geq 10^{17}$ cm^{-2} and $r \simeq 3.9 \pm 0.7 \times 10^8$ cm (see Model 5 in Table 1). Other density-sensitive lines from Fe XX and Fe XXI contribute to the density determination in fits with photoioniozation models. Numerous details and possibilities are explored below, but the most sound and important result of this analysis is that X-ray absorption has been detected within approximately 5000 km from a compact object that is likely a black hole.

It is nominally possible that the source harbors a white dwarf and that the spectrum originates in some sort of photosphere; however, this is extremely unlikely. The temperature of the continuum emission is far more consistent with accretion onto a neutron star or black hole; so too is the hard X-ray component detected in MAXI J1305−704. No X-ray bursts nor pulsations have been reported in observations of MAXI J1305−704, nor has timing behavior characteristic of many neutron star X-ray binaries (e.g. strong low–frequency QPOs.). If the source is a neutron star, Model 5 constrains the absorption to occur within $r = 1700\ r_g$ for a neutron star with $M = 2\ M_\odot$. This is already very small, even by the standards of X-ray winds in binaries. However, the optical spectrum and X-ray flux changes observed in MAXI J1305−704 are suggestive of a black hole primary. In that case, the absorption originates at or within $520 \pm 90(M/5\ M_\odot)\ r_g$. The disk wind in GRO J1655−40 is also dense, and likely launched at similar radii (based on fits to the Fe K band in Miller et al. 2008, as well as models including a higher velocity component in Kallman et al. 2009). The disk wind in H 1743−322 may originate at similar radii, though the constraints allow for larger radii (Miller et al. 2006). If the speed of the "ultra-fast" outflow found in IGR J17091−3624 reflects its local escape velocity, then it too originates at approximately $10^3\ r_g$ (King et al. 2012).

At such small launching radii, gravitational red-shifts are non-negligible. Appoximating the shift as $v/c = z \simeq GM/rc^2$ and taking r = 3000–8000 km (see Models 1, 4, 5, 8, 9, and 12 in Table 1), $z = 0.9 - 2.5 \times 10^{-3} M_5$ is expected. Red-shifts that are broadly consistent with this range are measured from each of the models in Table 1 with variable density values. This could be explained in terms of gas that is executing orbital motion relatively close to the black hole, that has been lifted above the plane of the disk, but is not escaping.

When two-zone models are explored, vastly better fits are achieved, and a much larger red-shift is measured in the additional component. Models 4, 8, and 12 include zones with $v/c = z = 4.6 - 4.9 \times 10^{-2}$. It is worth noting that shifts this large could affect the density constraints obtained from the Fe XXII line pair, because the 11.77 Å line from the more shifted zone can begin to contribute to the 11.92 Å line from the less shifted zone. In Models 4 and 8, good constraints were still achieved for both zones, and $n \geq 10^{17}$ cm^{-3} is required. In Model 12, however, a value consistent with $n = 10^{16}$ cm^3 is measured. Model 8 has the advantage of applying to a fairly large wavelength range while still concentrating on the Fe XXII lines, but Model 12 may represent the best overall description of the spectrum (this is certainly true in terms of χ^2). This larger shift seen in the second zone in these models is broadly consistent with the free–fall velocity at the radius required by photoionization modeling. Taking $M_{BH} = 5\ M_\odot$ and $r = 520\ r_g$, for instance, $z = 6.2 \times 10^{-2}$ is expected. The gas need not fall from infinity; traversing a distance comparable to the absorption radius would give a shift similar to the full local free–fall velocity. The fact that the measured shifts may be slightly below the full free–fall velocity may support a picture wherein gas has travelled only locally.

Figure 7 shows that these shifts – if they reflect a gravitational red-shift and free–fall velocity – can be realized over a common set of radii for plausible compact object masses. This is only marginally possible for a neutron star with $M_{NS} = 2.0\ M_\odot$, but easily possible for black holes fo a small mass. The results of fits to the spectrum of MAXI J1305−704 with XSTAR photionization models do not require that the two components originate at exactly the same radius in Model 12, but the two zones have overlapping radii for Models 4 and 8 (see Table 1).

Early observations of MAXI J1305−704 fueled speculation that the source may have a short orbital period, and so too have potential similarities with the short-period black hole XTE J1118+480 (e.g. Charles et al. 2012). Shidatsu et al. (2013) suggest a relatively short binary period of 9.74 ± 0.04 hours, based on an examination of flux dips. This would imply a short binary separation, and would help to explain the small absorption radius and high gas density implied by the data. The column density to MAXI J1305−704 is quite low, as noted above, and it is reasonable to expect that its period will be determined via optical methods in the near future.

"Failed winds" have been predicted in some simulations of accretion disks and winds in AGN, and they provide a natural explanation for our results (e.g. Proga & Kallman 2004, Proga 2005). Radiation pressure can launch winds when the Eddington fraction is sufficiently high and when the gas is self–shielding (this keeps the ionization low and enhances the force multiplier). However, if the force multiplier and/or Eddington fraction are too low, the gas cannot escape. Indeed, flows with inward velocity components – inflows – have been detected in the wind region in such simulations (Proga & Kallman 2004, Proga 2005).

If a "failed wind" has been detected in MAXI J1305−704, it may not be exactly like the flows predicted by recent simulations. Those studies examined accretion in AGN, wherein the disk emits most of its energy in the UV. Although the wind launching region in MAXI J1305−704 would correspond to a region emitting mostly in EUV if the disk follows the standard $T \propto r^{-3/4}$ prescription, the force multiplier is low for $\log(\xi) \simeq 2$–3, and this may mean that magnetic pressure is necessary even to lift the gas into the line of sight. As noted by Miller et al. (2008) in an analysis of the wind in GRO J1655−40, simulations predict that there should be ample magnetic flux for this purpose (e.g. Miller & Stone 2000).

It is interesting to note that the radius implied by photoionization modeling is commensurate with the radius at which warps may form. It is possible that a warp may help to lift gas up into the line of sight, or to shield gas from part of the flux from the central engine. At smaller radii, gravito-magneto-hydrodynamics is expected to anchor the disk in the plane perpindicular to the black hole spin axis, and to keep the disk flat (e.g. Bardeen & Petterson 1975; McKinney, Tchekhovskoy, & Blandford 2012). At larger radii, however, theoretical treatments suggest that warps can form and may be sustainable. Such warps might be expected to give rise to QPOs, and a connection between ionized absorption and QPO phase was detected in H 1743−322 (Miller et al. 2006). The frame time of the ACIS array is not suited to the detection of even slow QPOs in our observation, unfortunately, and we defer a timing analysis to later work on monitoring observations with *Swift*.

Failed winds may drive an emerging anti-correlation between winds and jets, by interfering with the formation or maintenance of a hard X-ray corona. Observations clearly signal that disk winds are observed in soft, disk–dominated states in which the jet is quenched (Miller et al. 2006, 2008, 2012; Neilsen & Lee 2009; King et al. 2012; Ponti et al. 2012). In constrast, compact, steady jets are ubiquitous in low–flux, spectrally–hard states wherein coronal emission dominates disk emission. As noted by Proga (2005), infusing the region above the disk with too much cool gas can interfere with a hot, optically–thin, Comptonizing corona. Connections between X-ray flux and radio flux are typically corona–jet connections, not true disk–jet connections, since X-ray monitors do not typically detect the cool disk emission that is found in the low/hard state (see, e.g., Reis, Miller, & Fabian 2010). In the one case where the role of the disk has been examined directly, it is found not to play a strong role, and the results suggest that the corona is the base of the relativistic radio jet (Miller et al. 2012d, also see Reis & Miller 2013). Winds that flow inward might have a profound effect on the corona, and thus the base of a would–be jet.

A shortcoming of this scenario stems from the issue of ionization. It is possible that magnetic pressure is needed for a failed wind, just as it is required to drive the wind seen in GRO J1655−40 (Miller et al. 2006, 2008; Kallman et al. 2009; Neilsen & Homan 2012; Neilsen 2013). Given that jets are commonly thought to be powered via magnetic fields that tap the rotation of the disk (or the spin of the black hole, or both), given that some winds may be magnetic (as deduced via a small launching radius, or a mass outflow rate exceeding the expected range for thermal winds, or both), and given recent work showing that winds and jets might be powered and regulated in a common fashion (King et al. 2013), it is possible that radiation pressure does not enter into the disk–wind–jet connection. A more modest conclusion is that radiation pressure

may be unimportant in X-ray binaries. This also follows from the high ionization parameters observed in X-ray binaries, and simulations that show no force multiplier above $\log(\xi) \simeq 3$ (e.g. Proga 2003). In their study of GRO J1655−40, Miller et al. (2008) note that magnetic pressure from MRI processes may be a more likely driver than magnetocentrifugal forces (also see Neilsen 2013), and that the wind/jet dichotomy may be driven by changes between a primarily toroidal field in disk–dominated soft states, and a primarily poloidal field in corona–dominated hard states with relativistic jets.

It is possible that other physical scenarios could give the observed absorption spectrum and velocity shifts. For instance, the more strongly shifted, potentially infalling gas could originate in the outer disk. If the accretion stream onto the outer disk overflows, as per some observations and simulations of interacting binaries (e.g. Armitage & Livio 1996), some gas may fall inward relatively independently of the accretion disk. van Peet et al. (2009) discussed an overflow scenario like this, as a possible explanation for the Fe L absorption detected in the neutron-star X-ray binary EXO 0748−676. In this case, dips might originate when material still in the outer disk – close to the point of impact – passes across the line of sight; absorption seen in steady phases (as with this observation of MAXI J1305−704 and some phases of EXO 1748−676) would arise via stream material that had fallen into the inner disk. If this is correct, the broadly similar properties of the potentially free-falling gas in MAXI J1305−704, and the gas that might be partly rotationally–supported, would be largely coincidental. Moreover, Armitage & Livio (1996) note that overflow would be less likely when the disk is hot and vertically extended, as per a sitation that might arise when the accretion rate is high and irradiation is important. The hot disk temperature indicated in MAXI J1305−704 indicates a rather high Eddington fraction, which is always accompanied by irradiation (Reynolds & Miller 2013). For these reasons, we favor a failed wind scenario.

Although a fairly simple and self–consistent picture can be developed to explain the data, and though the red–shifts observed are natural to the radius implied by photoionization modeling, the red-shifts must be regarded skeptically. These shifts have not previously been detected at high statistical confidence in any accretion–powered system. Moreover, this observation differs from others in that it has a large pointing offset, and it is possible that the shifts are instrumental.

We attempted to test this possibility by simulating this observation using the *Chandra*/MARX ray-tracing packgage. Those simulations suggest that the red-shifts are not instrumental in origin; however, MARX is only as good as the instrument data and characterizations that drive it. If its assumptions are incorrect, or if they are limited in their scope, then MARX may not deliver the correct results for our observation of MAXI J1305−704.

We also attempted to make simple tests of the red-shifts by analyzing the zeroth-order ACIS-S3 spectrum, which should not be affected in the same manner as the dispersed spectra. Again, the test suggests that the red-shifts are not instrumental (see Table 1), but CCD spectra have only moderate resolution and the results are not definitive. Thus, an instrumental origin for the observed shifts remains a remote possibility. Fortunately, the radius implied by photoionization modeling, and requirement of a high gas density, are unaffected by any issues related to velocity shifts. So too, then, is the potential association of this gas with a failed wind, and the implications of failed winds for jet production and state transitions.

The neutral ISM along the line of sight might, in different circumstances, have provided a natural check of the wavelength calibration of this spectrum. However, the column density along the line of sight to MAXI J1305−704 is very low (we adopted $N_H = 1.5 \times 10^{21}$ cm^{-2}), and this means strong ISM lines will not be imprinted on the spectrum. Cases where strong ISM lines have been observed typically have measured column density values that are a factor of a few higher (e.g. Pinto et al. 2013). The absorption spectrum detected within MAXI J1305−704 is then approximately an order of magnitude greater in column density than the ISM along this line of sight (see Table 1). The wind column dominated the potential ISM column and effectively spoiled a natural wavelenth calibration. Among the non–Fe lines that are detected and not clearly blended, including the O VIII Ly-α and Ly-β lines, and the Ne IX He-α line, fits with simple Gaussians find the same $v/c \simeq 3 \times 10^{-3}$ shift that is measured in photoioniztion models dominated by Fe L transitions.

If the red-shifts detected in MAXI J1305−704 are astrophysical, they are exceptional. It is worth noting, though, that MAXI J1305−704 is exceptional in other ways as well, and that such shifts may be somewhat less remarkable in this source. Other X-ray binares, and other "dippers", have also shown interesting X-ray absorption spectra. But as noted by Diaz-Trigo (2006), the gas is typically very highly ionized, with the most pronounced effects in the Fe K band. Among X-ray binaries, MAXI J1305−704 is rare in showing such a rich and complex absorption spectrum in the Fe L band, whether in or out of a dip phase (also see the spectrum of EXO 0748−676 analyzed by van Peet et al. 2009). Other sources viewed at high inclination show substantially different spectra, dominated by emission lines; the differences might be dictated by exactly how high the inclination is. Her X-1, for instance, shows a complex emission line spectrum (e.g. Jimenez-Garate et al. 2002). So too do other so-called "accretion disk coronae" sources, including e.g. 2S 0921−63 (Kallman et al. 2003). Future observations of MAXI J1305−704 and other black hole candidates with *Chandra*, *XMM-Newton*, and eventually *Astro-H* (Takahashi et al. 2012) can help to reveal the dynamics and physics of wind and jet production and to confirm possibilities such as red-shifts and Doppler-split line pairs.

REFERENCES

Armitage, P. J., & Livio, M., 1996, ApJ, 470, 1024

Arnaud, K. A., and Dorman, B., 2000, XSPEC is available via the HEASARC on-line service, provided by NASA/GSFC

Bardeen, J. M., & Petterson, J. A., 1975, ApJ, 195, L65

Begelman, M. C., McKee, C. F., & Shields, G. A., 1983, ApJ, 271, 70

Blandford, R. D., & Payne, D. G., 1982, MNRAS, 199, 883

Charles, P., Cornelisse, R., Foster, D., Casares, J., Kotze, M., Zdziarski, A., 2012, ATEL 4105

Coriat, M,. Broderick,J., Tzioumis, T., Fender, R., Corbel, S., Brocksopp, C., Breton, R., 2012, ATEL 4067

Diaz-Trigo, M., Parmar, A. N., Boirin, L., Mendez, M., Kaastra, J. S., 2006, A&A, 445, 179

Greiner, J., Rau, A., & Schady, P., 2012, ATEL 4030

Jimenez-Garate, M. A., Hailey, C. J., den Herder, J. W., Zane, S., Ramsay, G., 2002, ApJ, 578, 391

Juett, A. M., Schulz, N. S., Chakrabarty, D., Gorczyca, T. W., 2006, ApJ, 648, 1066

Kallman, T. R., Anglelini, L., Boroson, B., & Cottam, J., 2003, ApJ, 583, 861

Kallman, T. R., Bautista, M. A., Goriely, S., Mendoza, C., Miller, J. M., Palmeri, P., Quinet, P., Raymond, J., 2009, ApJ, 701, 865

Kallman, T. R., & Bautista, M., 2001, ApJS, 133, 221

Kennea, J. A., Altamirano, D., Evans, P. A., Krimm, H. A, Romano, P., Mangano, V., Curran, P., Yamaoka, K., Negoro, H., 2012, ATEL 4034

Kennea, J. A., Miller, J. M., Beardmore, A., Degenaar, N., & Reynolds, M. T., 2012, ATEL 4071

King, A. L., Miller, J. M., Raymond, J., 2012, ApJ, 746, 2

King, A. L., et al., 2012, ApJ, 746, L20

King, A. L., Miller, J. M., & Raymond, J., 2012, ApJ, 746, 2

King, A. L., Miller, J. M., Raymond, J., Fabian, A. C., Reynolds, C. S., Gultekin, K., Cackett, E. M., Allen, S. W., Proga, D., Kallman, T. R., 2013, ApJ, 762, 103

Kubota, A., et al., 2007, PASJ, 59, 185

Kuulkers, E., Motta, S., Belloni, T. M., 2012, ATEL 4073

Madej, O., & Jonker, P, 2011, MNRAS, 412, L11

Madej, O., Jonker, P., & Fabian, A. C., 2010, MNRAS, 407, L11

Mauche, C., Liedahl, D., & Fournier, K., 2003, ApJ, 588, L101

McKinney, J. C., Tchekhovskoy, A., & Blandford, R. D., 2012, Science, 339, 49

Migliari, S., & Fender, R. P., 2006, MNRAS, 366, 79

Miller, J. M., et al., 2006, ApJ, 646, 394

Miller, J. M., et al., 2006, Nature, 441, 953

Miller, J. M., et al., 2008, ApJ, 680, 1359

Miller J. M., Maitra, D., Cackett, E. M., Bhattacharyya, S., Strohmayer, T. E., 2011, ApJ, 731, L7

Miller, J. M., Raymond, J., Fabian, A. C., Reynolds, C. S., King, A. L., Kallman, T. R., Cackett, E. M., van der Klis, M., Steeghs, D. T. H., 2012, ApJ, 759, L6

Miller, J. M., Beardmore, A., Kennea, J., Reynolds, M. T., King, A. L., Fabian, A. C., Reynolds, C. S., & Raymond, J. C., 2012b, ATEL 4070

Miller, J. M., Beardmore, A., Kennea, J., Reynolds, M. T., King, A. L., Fabian, A. C., Reynolds, C. S., Raymond, J., 2012b, ATEL 4070

Miller, J. M., Raymond, J., Kennea, J., Beardmore, A., Reynolds, M. T., Maitra, D., Degenaar, N., Cackett, E. M., Fabian, A. C., Reynolds, C. S., 2012c, ATEL 4191

Miller, J. M., Pooley, G., Fabian, A. C., Nowak, M. A, Reis, R. C., Cackett, E. M., Pottschmidt, K., & Wilms, J., 2012, ApJ, 757, 11

Miller, K. A., & Stone, J. M., 2000, ApJ, 534, 398

Mitsuda, K., et al., 1984, PASJ, 36, 741

Neilsen, J., 2013, Proceedings of the 39th COSPAR Assembly, Mysore, India, AdSpR, in press, arxiv:1305:6091

Neilsen, J., & Homan, J., 2012, ApJ, 750, 27

Neilsen, J., Lee, J. C., 2009, Nature, 458, 481

Nikolic, D., Gorczyca, T.W., Korista, K.T., Ferland, G.J. & Badnell, N.R. 2013, ApJ, 768, 82

Pinto, C. Kaastra, J. S., Costantini, E., de Vries, C., 2013 A&A, 551, 25

Ponti, G., Fender, R. P., Begelman, M. C., Dunn, R. J. H., Neilsen, J., Coriat, M., 2012, MNRAS, 422, L11

Proga, D., 2003, ApJ, 585, 406

Proga, D., 2005, ApJ, 630, L9

Proga, D., & Kallman, T. R., 2004, ApJ, 616, 688

Reis, R., Fabian, A. C., & Miller, J. M., 2010, MNRAS, 402, 836

Reis, R., & Miller, J. M., 2013, ApJ, 769, L7

Reynolds, C. S., 2012, ApJ, 759, L15

Rykoff, E. S., Miller, J. M., Steeghs, D., & Torres, M. A. P., 2007, ApJ, 666, 1129

Sato, R., et al., 2012, ATEL 4024

Shakura, N. I., & Sunyaev, R. A., 1973, A& A, 86, 121

Shidatsu, M., et al., 2013, ApJ, 779, 26

Suwa, F., et al., 2012, ATEL 4035

Takahashi, T., et al., 2012, SPIE, 8443, 1

Ueda, Y., Murakami, H., Yamaoka, K., Dotani, T., Ebisawa, K., 2004, ApJ, 609, 325

Ueda, Y., Yamaoka, K., Remillard, R., 2009, ApJ, 695, 888

van Peet, J. C. A., Constantini, E., Mendez, M., Paerels, F. B. S., Cottam, J., 2009, A&A, 497, 805

Verner, Verner, & Ferland 1996, 64,1

Wilms, J., Allen, A., & McCray, R., 2000, ApJ, 542, 914

TABLE 1
PHOTOIONIZATION MODELING RESULTS

Model	Range	Notes	χ^2/ν	n (10^{17} cm^{-3})	N_H (10^{22} cm^{-2})	$\log(\xi)$	v/c (10^{-3})	r (10^8 cm)
1	11.2–13.2 Å	1-zone, free n	868/384	4(2)	0.80(6)	2.03(2)	3.0(2)	5(2)
2		1-zone, fixed n	878/385	0.5	0.75(5)	2.05(3)	2.9(2)	13(1)
3		1-zone, fixed n	896/385	0.1	0.66(5)	2.05(3)	2.7(3)	30(1)
4	11.2–13.2 Å	2-zone, free n	715/380	2.1(6)	1.3(4)	2.60(7)	2.8(3)	4(1)
				5(2)	0.67(5)	$2.00^{+0.01}$	47(1)	4.7(9)
5	10.0–14.0 Å	1-zone, free n	1647/785	6(1)	1.05(3)	2.05(2)	2.8(2)	3.9(7)
6		1-zone, fixed n	1683/786	0.5	0.97(3)	2.08(1)	2.3(2)	13(1)
7		1-zone, fixed n	1716/786	0.1	0.85(3)	2.07(2)	2.1(2)	29(1)
8	10.0–14.0 Å	2-zone, free n	1434/779	2.2(4)	1.27(5)	2.60(2)	2.3(2)	3.4(7)
				7(2)	0.70(4)	$2.00^{+0.04}$	47.0(3)	3.9(7)
9	8.0-19.5 Å	1-zone, free n	4537/2286	1.1(1)	1.22(4)	2.36(1)	2.8(2)	6.3(6)
10		1-zone, fixed n	4552/2287	0.5	1.20(3)	2.36(1)	2.5(2)	9.3
11		1-zone, fixed n	4588/2287	0.1	1.08(3)	2.37(1)	2.2(1)	20.9
12	8.0-19.5 Å	2-zone, free n	3378/2280	0.7(2)	1.10(5)	2.62(1)	1.8(2)	6(2)
				$0.10^{+0.05}$	0.55(5)	2.65(1)	48(1)	15.0
13	3.0-10.0 keV	1-zone, fixed	592/474	0.7	1.1	2.62	1.8	5.9
14		1-zone, free	536/471	1.0	6(2)	4.0(1)	<2	1.0
15	3.0-10.0 keV	2-zone, mixed	534/471	0.7	1.1	2.62	1.8	5.9
				5	1.2(4)	4.4(1)	22(1)	0.3
16	3.0-10.0 keV	2-zone, free	509/468	1.0	6(2)	4.0(1)	<2	1.0
				1.0	6(2)	4.3(1)	21(3)	0.7

NOTE. — The table above details the results of fits with a large grid of XSTAR photoionization models (see the text for additional details). Single-zone fits, models with a fixed (artificially low) density, and two-zone models for the combined first-order MEG spectrum were considered on three different wavelength ranges. The results of fits to the zeroth-order ACIS-S3 CCD spectrum on the 3–10 keV band are included in the final segment of the table. The errors listed in the table are 1σ confidence intervals. Symmetric errors are given in parentheses. Where errors are not given, the parameter was fixed. Positive velocities indicate a red-shift. Single-zone fits clearly prefer a high density, and the addition of a second zone gives a significantly improved fit over all three fitting ranges. Errors are not quoted on radii derived via fits to the ACIS-S3 spectrum because the density was fixed in those models. None of the models above provide formally acceptable fits in a statistical sense, similar to the situation in complex optical and UV spectra, and in fits to the X-ray spectrum of GRO J1655–40 (e.g. Miller et al. 2008). However, the relative efficacy different models can still be easily gauged through the comparison of χ^2 fit statistics.

TABLE 2
STRONG ABSORPTION LINES IN MAXI J1305−704

Ion and Transition	Lab Wavelength (Å)
O VIII 1s–3p	15.987
O VIII 1s–2p	18.9689
Ne IX $1s^2$–1s4p	11.0003
Ne IX $1s^2$–1s3p	11.5466
Ne IX $1s^2$–1s2p	13.447
Ne X 1s–6p	9.3616
Ne X 1s–5p	9.4807
Ne X 1s–4p	9.7082
Ne X 1s–3p	10.2389
Ne X 1s–2p	12.1330
Na XI 1s–2p	10.0250
Mg XII 1s–2p	8.4210
Mg XI $1s^2$–1s2p	9.1688
Fe XIX $2s^2 2p^4$–$2s^2 2p^3$3d	13.520
Fe XX $2s^2 2p^4$–$2p^2(^3P)$4d	9.991
	10.12
Fe XX $2s^2 2p^4$–$2p^2(^3P)$3d	12.82
Fe XXI $2s^2 2p^2$–$2s^2$2p3d	12.259
	12.325
Fe XXII $2s2p^2$–2s2p4d	9.163
	9.183
Fe XXII $2s^2 2p$–$2s^2$3d	11.770
	11.920
Fe XXIII $2s^2$–2s4p	8.3029
Fe XXIII $2s^2$–2p3d	10.175
Fe XXIII $2s^2$–2p3s	10.560
Fe XXIII $1s^2 2s^2$–$1s^2$2s3p	10.980
Fe XXIII $1s^2 2s2p$–$1s^2$2s3p	11.018
Fe XXIV $1s^2 2s$–$1s^2$3p	10.619
	10.663

NOTE. — The table above lists lines that likely contribute strongly to the absorption spectrum observed in MAXI J1305−704 in the 8–19.5 Å band, based on modeling with XSTAR photoionization calculations. The quoted wavelengths are taken from Verner, Verner, & Ferland (1996) and the NIST Atomic Spectrsocopy Database. The transitions associated with the lines at 10.175 Å and 10.560 Å should be regarded as tentative. The density of lines in the MEG band considered in this analysis, the slightly degraded resolution of the MEG spectrum, and the intrinsic width of the lines serve to create some line blends. While a self-consistent photoionization model can handle this situation, line-by-line fitting with simple Gaussians cannot. In addtion, some lines are saturated, meaning that velocity widths would effectively be upper-limits and line fluxes would be lower-limits. Thus, individual line widths and fluxes are not quoted. Relatively simple one- and two–zone photoionization models are described in Table 1.
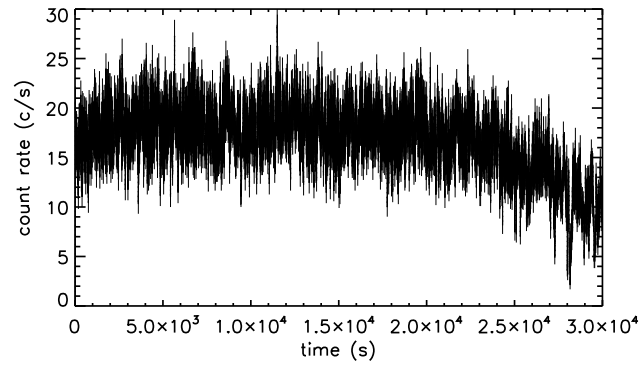
FIG. 1.— The figure above shows the light curve of MAXI J1305−704, derived using 0.3–10.0 keV photons in the first-order MEG and HEG. The time bins are 10 s (longer than the nominal 3.2 s ACIS frame time) in order to improve visual clarity. The light curve shows variability typical of accreting low-mass X-ray binaries, with slightly lower flux levels at the start and end of the observation.
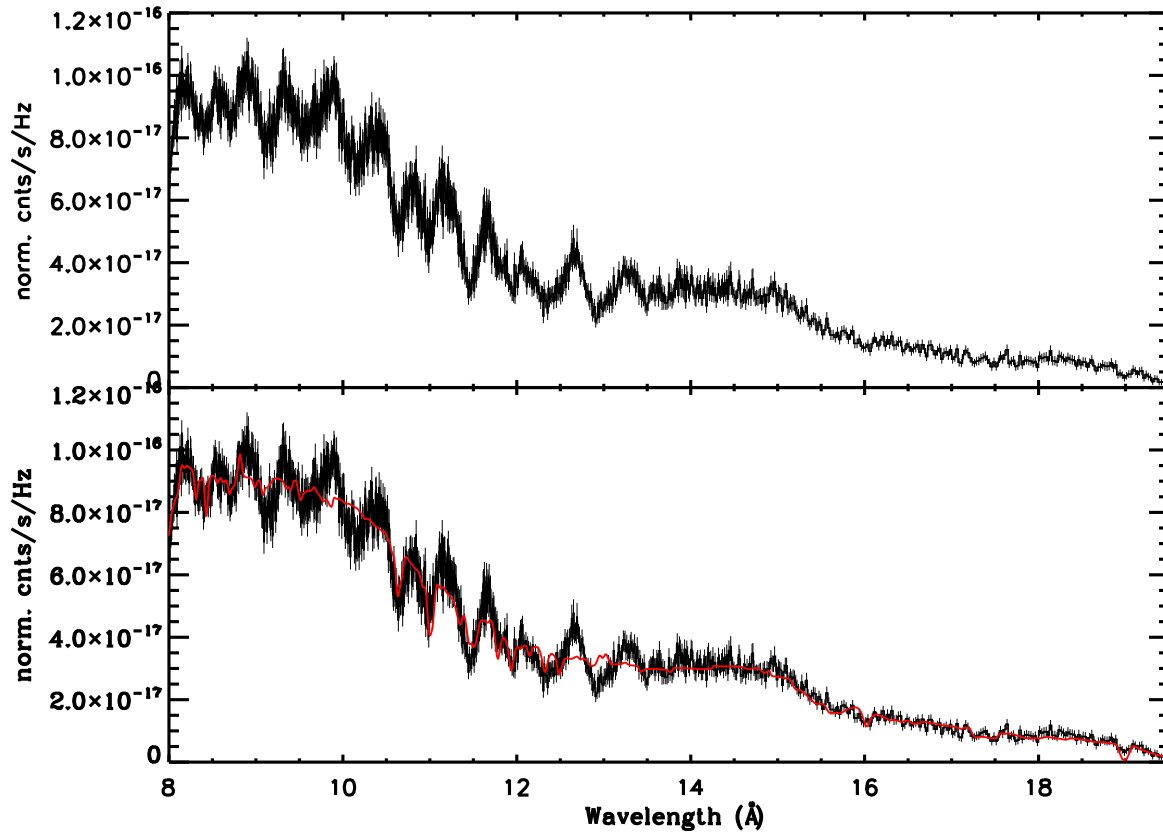
FIG. 2.— The figure above shows the 8–19.5 Å combined first-order MEG spectrum of MAXI J1305−704. The top panel shows the raw spectrum. The bottom panel shows the best-fit two-zone absorption model, generated using a very large XSTAR grid (Model 16 in Table 1 is shown). The plots are not "fluxed" to avoid bias, but the spectra have been binned for visual clarity. Absorption due to H-like O VIII is visible at 19 Å (Ly-α) and 16 Å (Ly-β); most of the other features are Fe L-shell transitions.
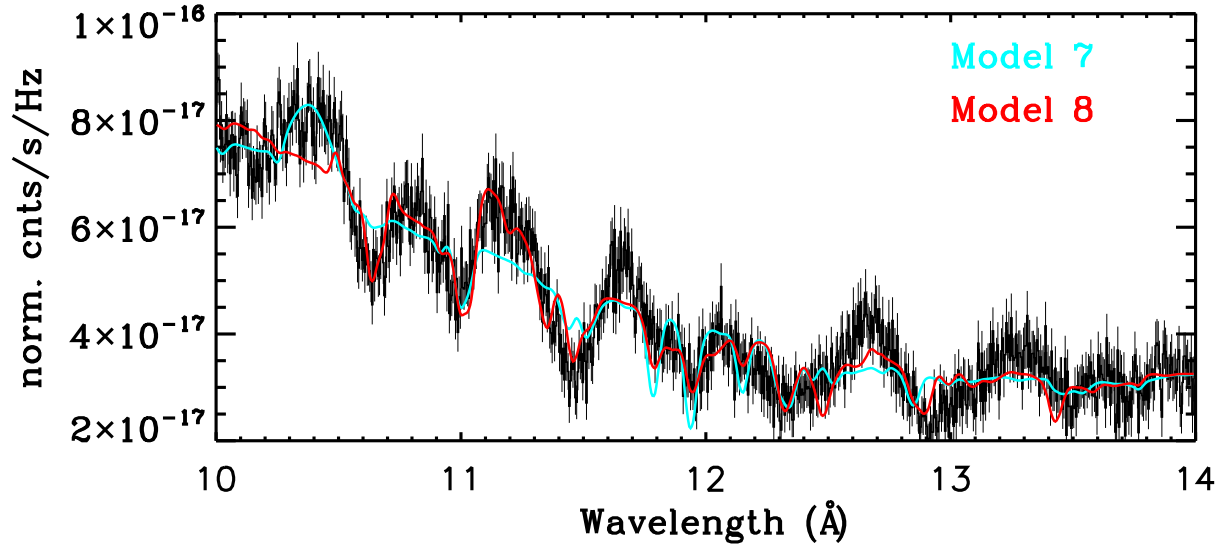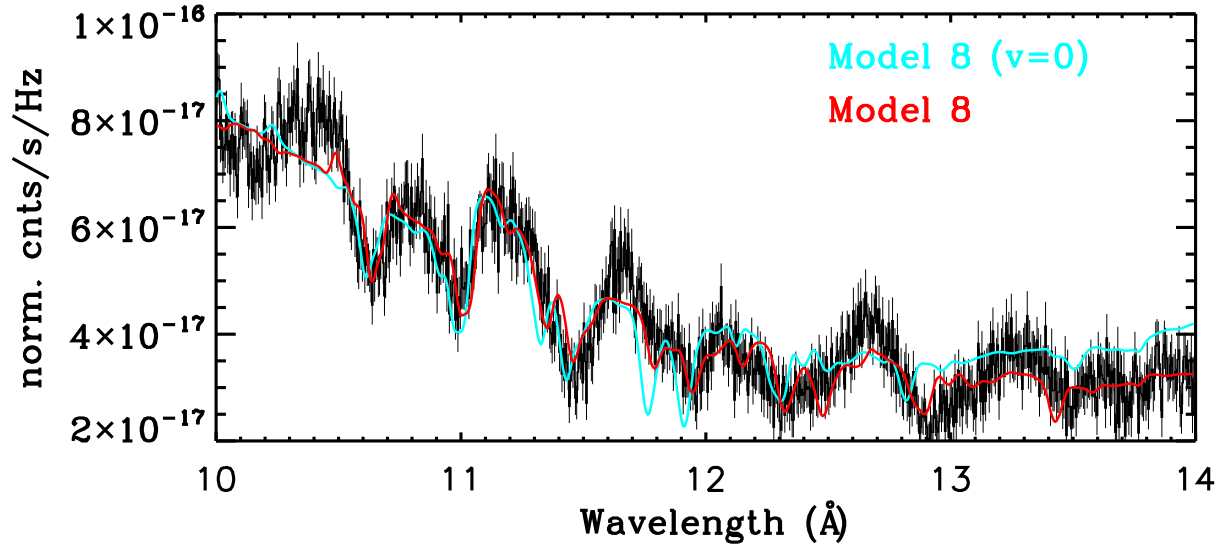
FIG. 3.— The figure above shows the combined first-order MEG spectrum of MAXI J1305−704 in the 10–14 Å region, roughly centered on the density-sensitive Fe XXII lines (laboratory wavelengths: 11.77 Å, 11.92 Å). Model 7 is a single-zone absorption model wherein the density is fixed at $n = 1.0 \times 10^{16}$ cm^{-3} (see Table 1); it is plotted in cyan. Model 8 is a two-zone absorption model with variable (high) densities that yields a significantly improved fit; it is shown in red. Note that the Fe XXII lines are fit much better with Model 8, as well as the lines at approximately 10.6 Å, 11.5 Å, and the complex near to 12.9 Å. The plot has not been "fluxed" to avoid bias, but the spectra have been binned for visual clarity.

FIG. 4.— The figure above shows the combined first-order MEG spectrum of MAXI J1305−704 in the 10–14 Å region, roughly centered on the density-sensitive Fe XXII lines (laboratory wavelengths: 11.77 Å, 11.92 Å). Model 8 is shown in red as presented in Table 1. It is also plotted in cyan after setting the velocity of both absorption components to zero. Clearly, the velocity shifts are important in obtaining robust fits to the spectrum. The plot has not been "fluxed" to avoid bias, but the spectra have been binned for visual clarity.
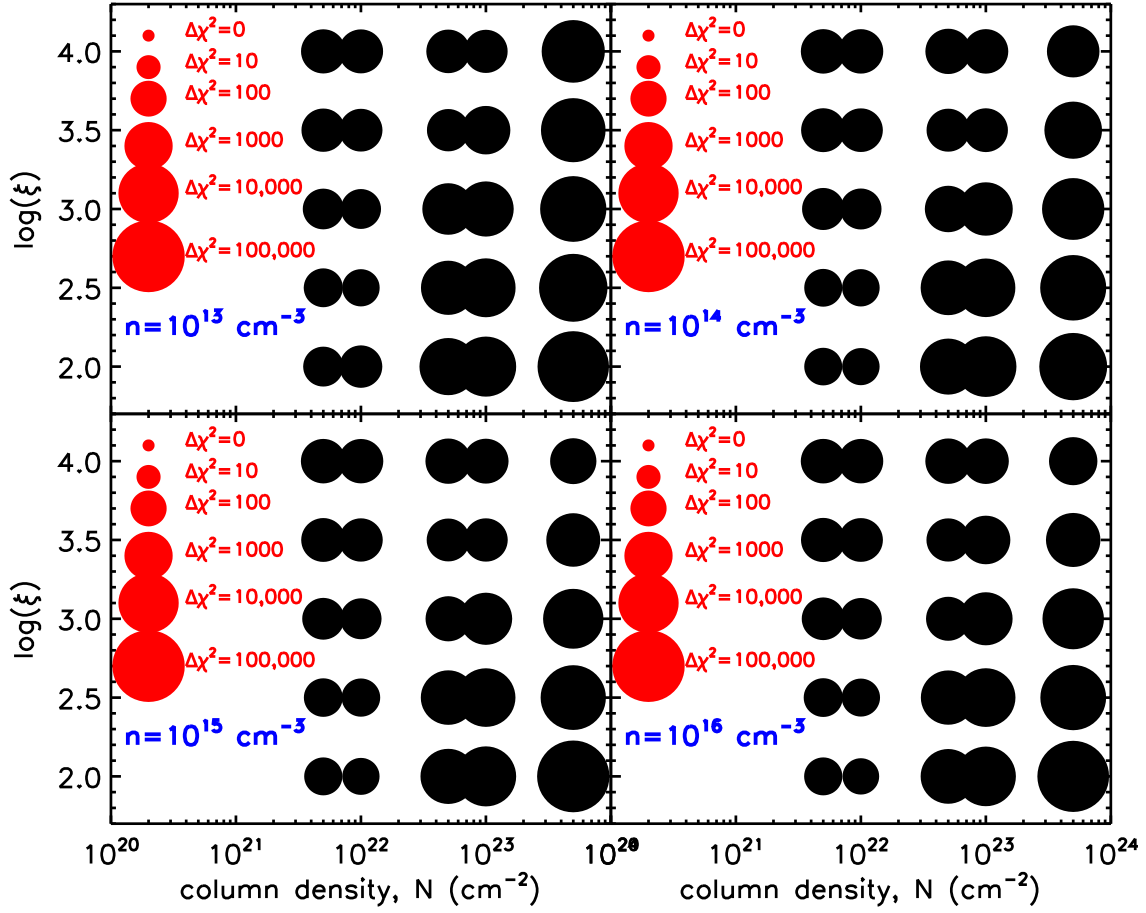
FIG. 5.— The figure above shows the result of single–zone fits to the 10–14 Å region using XSTAR photoionization models. Each panel shows the results of fits with 25 different combinations of ionization paramter ξ and column density N_H, for a specific value of the gas density. The size of the plotting symbol depicts a logarithmic scale in $\Delta(\chi^2)$ versus the best–fit single–zone absorber (Model 5 in Table 1; $n = 6 \pm 1 \times 10^{17}$ cm^{-3}). This exploration of a broad three–dimensional parameter space shows that any fit with a low density gives $\Delta(\chi^2) > \sim 100$. Indeed, in many cases, $\Delta(\chi^2) > 1000$. This exercise demonstrates that a very high density is required to fit the spectrum of MAXI 1305−704.
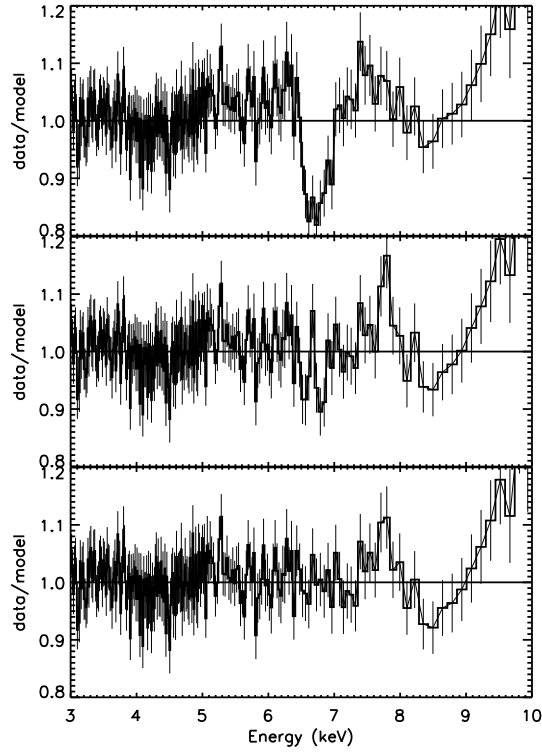
FIG. 6.— The plot above shows the data/model ratios resulting from three fits to the zeroth-order ACIS spectrum of MAXI J1305−704. The top panel shows a simple fit without absorption. The middle panel shows a single-zone absorber with all parameters free, apart from $n = 1.0 \times 10^{17}$ cm^{-3} (Model 14 in Table 1). Note that residuals consistent with slightly red-shifted Fe XXV and XXVI remain. The bottom panel shows a fit with two absorption zones; the second is significantly red-shifted (see Model 16 in Table 1). Different tests find that the inclusion of a second, red-shifted absorber is significant at the 4–6σ level of confidence. The data were binned for visual clarity. The flux excess above 9 keV is due to pile-up. In each case, the continuum model is fiducial.
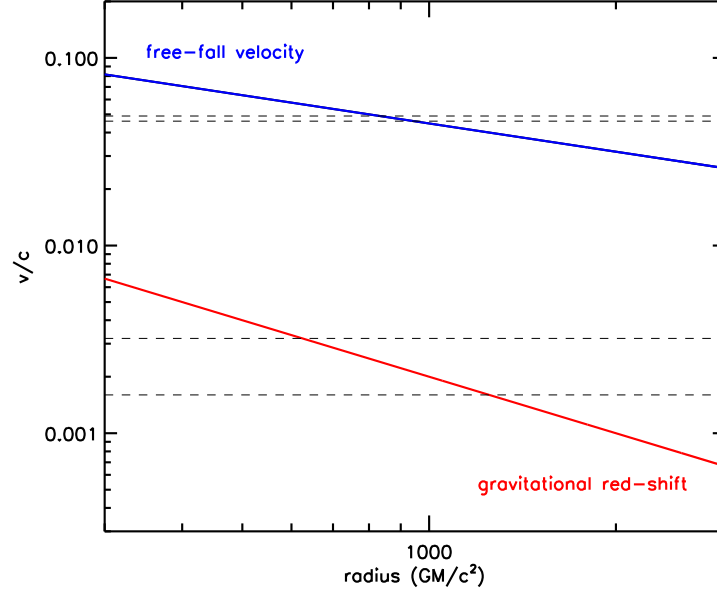
F<small>IG</small>. 7.— The plot above shows the dependence of free–fall velocity (in blue) and gravitational red-shift velocity (in red), as a function of radius. The dashed horizontal lines indicate the range of velocity shifts detected in fits to the MEG spectrum of MAXI J1305−704 via fits with both single–zone and two–zone XSTAR photoionization models with variable gas density parameters. Those same photoionization models require that the absorption occur at a distance of $r = 3.9 \pm 0.7 \times 10^3$ km from the compact object. This radius corresponds to 1300 GM/c^2 for a neutron star with $M = 2.0\ M_\odot$; this only just intersects the range for which the two velocities can be observed at a common radius. For black holes with masses of $M \leq 5 M_\odot$, $r = 3.9 \pm 0.7 \times 10^3$ km corresponds to radii for which the two velocities can be observed at a common distance from the central engine. Other uncertainties, for instance in the luminosity, would allow for greater overlap in the radii implied by each velocity shift.